

Article

Energy Transfer and Cross-Relaxation Induced Efficient 2.78 μm Emission in $\text{Er}^{3+}/\text{Tm}^{3+}$: PbF_2 mid-Infrared Laser Crystal

Jiayu Liao ^{1,2,3,†}, Qiudi Chen ^{1,2,3,†}, Xiaochen Niu ^{1,2,3}, Peixiong Zhang ^{1,2,3,*}, Huiyu Tan ^{1,2,3}, Fengkai Ma ^{1,2,3}, Zhen Li ^{1,2,3}, Siqi Zhu ^{1,2,3}, Yin Hang ⁴, Qiguo Yang ⁵ and Zhenqiang Chen ^{1,2,3}

- ¹ Guangdong Provincial Key Laboratory of Optical Fiber Sensing and Communications, Guangzhou 510630, China; jylio@stu2019.jnu.edu.cn (J.L.); Cqd596918045@163.com (Q.C.); nxc_n1u@163.com (X.N.); thy@stu2020.jnu.edu.cn (H.T.); hkai80@163.com (F.M.); ailz268@126.com (Z.L.); tzhusiqi@jnu.edu.cn (S.Z.); tzqchen@jnu.edu.cn (Z.C.)
 - ² Guangdong Provincial Engineering Research Center of Crystal and Laser Technology, Guangzhou 510632, China
 - ³ Department of Optoelectronic Engineering, Jinan University, Guangzhou 510632, China
 - ⁴ Key Laboratory of High Power Laser Materials, Shanghai Institute of Optics and Fine Mechanics, Chinese Academy of Sciences, Shanghai 201800, China; yhang@siom.ac.cn
 - ⁵ Guangdong Provincial Key Laboratory of Industrial Ultrashort Pulse Laser Technology, Shenzhen 518055, China; yangqiguo@126.com
- * Correspondence: pxzhang@jnu.edu.cn
† These authors contribute equally to this work.



Citation: Liao, J.; Chen, Q.; Niu, X.; Zhang, P.; Tan, H.; Ma, F.; Li, Z.; Zhu, S.; Hang, Y.; Yang, Q.; et al. Energy Transfer and Cross-Relaxation Induced Efficient 2.78 μm Emission in $\text{Er}^{3+}/\text{Tm}^{3+}$: PbF_2 mid-Infrared Laser Crystal. *Crystals* **2021**, *11*, 1024. <https://doi.org/10.3390/cryst11091024>

Academic Editors: Ludmila Isaenko and Anna Paola Caricato

Received: 22 July 2021

Accepted: 24 August 2021

Published: 26 August 2021

Publisher's Note: MDPI stays neutral with regard to jurisdictional claims in published maps and institutional affiliations.



Copyright: © 2021 by the authors. Licensee MDPI, Basel, Switzerland. This article is an open access article distributed under the terms and conditions of the Creative Commons Attribution (CC BY) license (<https://creativecommons.org/licenses/by/4.0/>).

Abstract: An efficient enhancement of 2.78 μm emission from the transition of Er^{3+} : ${}^4\text{I}_{11/2} \rightarrow {}^4\text{I}_{13/2}$ by Tm^{3+} introduction in the Er/Tm : PbF_2 crystal was grown by the Bridgman technique for the first time. The spectroscopic properties, energy transfer mechanism, and first-principles calculations of as-grown crystals were investigated in detail. The co-doped Tm^{3+} ion can offer an appropriate sensitization and deactivation effect for Er^{3+} ion at the same time in PbF_2 crystal under the pump of conventional 800 nm laser diodes (LDs). With the introduction of Tm^{3+} ion into the Er^{3+} : PbF_2 crystal, the Er/Tm : PbF_2 crystal exhibited an enhancing 2.78 μm mid-infrared (MIR) emission. Furthermore, the cyclic energy transfer mechanism that contains several energy transfer processes and cross-relaxation processes was proposed, which would well achieve the population inversion between the Er^{3+} : ${}^4\text{I}_{11/2}$ and Er^{3+} : ${}^4\text{I}_{13/2}$ levels. First-principles calculations were performed to find that good performance originates from the uniform distribution of Er^{3+} and Tm^{3+} ions in PbF_2 crystal. This work will provide an avenue to design MIR laser materials with good performance.

Keywords: 2.78 μm mid-infrared emission; Er/Tm ; PbF_2 laser crystal; energy transfer mechanism; first-principles calculation

1. Introduction

Over the past several decades, mid-infrared (MIR) solid-state lasers operating around 2.7–3 μm have received extensive attention for numerous applications in medicine surgery, communications, remote sensing, pollution monitoring, and military countermeasures, etc. [1–5]. Additionally, 2.7–3 μm lasers are suitable pump sources for longer wavelength mid-infrared or long-infrared (8–12 μm) laser applications utilizing the optical parametric oscillators [6,7].

Up to now, many kinds of rare-earth ions in favorable ~ 3 μm MIR emissions have been analyzed, such as erbium ion (Er^{3+}): ${}^4\text{I}_{11/2} \rightarrow {}^4\text{I}_{13/2}$ [8], holmium ion (Ho^{3+}): ${}^5\text{I}_6 \rightarrow {}^5\text{I}_7$ [9], and dysprosium ion (Dy^{3+}): ${}^6\text{H}_{13/2} \rightarrow {}^6\text{H}_{15/2}$ [10]. Among them, the Er^{3+} ion-doped single crystal has been deemed as the effective source for ~ 3 μm laser operation, benefiting from its abundant energy levels, such as GSGG [11], YSGG [12], YAP [13], Lu_2O_3 [14], GdScO_3 [15], SrF_2 crystals [16], NdVO_4 [17], InVO_4 crystals [18], etc. As investigated, the Er^{3+} ion can be directly pumped utilizing 808 or 980 nm commercial laser diodes (LDs)

corresponding to Er³⁺ ion absorption transitions from ground state ⁴I_{15/2} to ⁴I_{9/2}, ⁴I_{11/2} levels, respectively. To take further advantage of this, a co-doping suitable sensitization ion having strong absorption around 980 nm or 800 nm would improve the absorption efficiency, such as Yb³⁺, Nd³⁺, or Tm³⁺ ions [19–21]. However, the fluorescence lifetime of the ⁴I_{11/2} level (the upper) is fairly shorter than that of the ⁴I_{13/2} level (the lower) of Er³⁺ ion, causing the possible termination of 2.7 μm mid-infrared emissions [22]. Therefore, the shortcoming of the intrinsic self-terminating “bottleneck” effect of Er³⁺ ion is important to consider. On one hand, the self-terminating “bottleneck” effect can be restrained by the energy transfer up-conversion (UC) process: 2 ⁴I_{13/2} → ⁴I_{15/2} + ⁴I_{9/2}, which needs heavy doping of Er³⁺ ion (>30 at.%). The UC process can simultaneously depopulate the ⁴I_{13/2} level and populate the ⁴I_{11/2} level via non-radiative transition from ⁴I_{9/2} to ⁴I_{11/2} levels. However, excessive Er³⁺ doping concentrations will generate the inclusion defects in as-grown crystal and degenerate the crystal quality and thermal performance, which is not conducive to laser output efficiency [23,24]. On the other hand, we can focus attention on co-doping a suitable deactivation ion for Er³⁺ ion to suppress the self-terminating effect, such as Pr³⁺, Ho³⁺, Dy³⁺, or Tm³⁺ ions [25–28]. These deactivation ions can dramatically reduce the population of lower Er³⁺: ⁴I_{13/2} levels, thereby achieving efficient 2.7 μm mid-infrared emission. Based on the above investigation, it is noteworthy that Tm³⁺ ion can simultaneously serve as sensitization and deactivation effects for Er³⁺ ion [29,30].

In recent years, fluoride crystals have attracted numerous attention in the field of mid-infrared lasers, such as the β-PbF₂ crystal [31]. The PbF₂ crystal exhibits its intrinsic advantages. The PbF₂ crystal has lower phonon energy (257 cm⁻¹), compared with GdLiF₄ (432 cm⁻¹), LiYF₄ (442 cm⁻¹), LuLiF₄ (400 cm⁻¹) and BaY₂F₈ (415 cm⁻¹) crystals [32–34]. Such low phonon energy is conducive to reducing the non-radiative transition probability and enhancing the spontaneous radiation transition probability between ⁴I_{11/2} and ⁴I_{13/2} levels of Er³⁺ ion [35]. Moreover, the PbF₂ crystal is optically transparent in the region of 0.25–15 μm, which is broader than other fluoride crystals, such as LiYF₄ (0.12–8.0 μm), BaY₂F₈ (0.2–9.5 μm), and KYF₄ (0.15–9.0 μm). Additionally, another issue to consider is the physical properties of the material. Some fluoride crystals have low thermal conductivity, such as CaF₂ and SrF₂. The PbF₂ crystal has high thermal conductivity (28 W/m/K) and stable mechanical and chemical properties [36,37]. Consequently, with these favorable characteristics, the PbF₂ crystal may be selected as a promising host material.

In this paper, Er: PbF₂, Tm: PbF₂, Er/Tm: PbF₂ crystals were successfully prepared by the Bridgman technique. The spectroscopic properties of prepared crystals were analyzed based on absorption spectra, emission spectra, and fluorescence decay curves. Compared with the Er: PbF₂ crystal, the Er/Tm co-doped PbF₂ crystal presents a larger 2.78 μm fluorescence emission intensity and higher fluorescence branching ratio. Moreover, theoretical calculations were performed to discover that the co-doping of the Tm³⁺ ion can make the Er³⁺ and Tm³⁺ ions more evenly distributed in PbF₂ crystals, which can effectively break the local clusters of the Er³⁺ in Er: PbF₂ crystal, thus ensuring efficient energy transfer between Er³⁺ and Tm³⁺ ions, and resulting in the enhancement of 2.78 μm MIR fluorescence emission.

2. Experimental Section

The 1.0 at.% Er: PbF₂, 0.5 at.% Tm: PbF₂, and 1.0 at.% Er/0.5 at.% Tm: PbF₂ crystals were grown by the conventional Bridgman method in an atmosphere of N₂ with intermediate molybdenum heating. The fluoride powders of the PbF₂ (99.999%), ErF₃ (99.999%), and TmF₃ (99.999%) were all raw materials. The raw materials were weighed and thoroughly mixed. The process of crystal growth was similar to our previous work [37]. The melt was homogenized in a covered graphite crucible in a high-temperature zone at 1000 °C for 8 h, and the crystal growth process was driven by lowering the graphite crucible at a speed of 0.5 mm/h. After the growth process was completed, the cooling rate of the crystal was 30 °C/cm–40 °C/h. The actual concentration of Er³⁺ and Tm³⁺ ions in the grown samples were measured utilizing inductively coupled plasma atomic emission

spectrometry (ICP-AES). The concentrations of Er^{3+} and Tm^{3+} ions in dual-doped Er/Tm: PbF_2 crystal were 1.15 at.%, and 0.58 at.%, respectively. The concentration of Er^{3+} ion in the Er: PbF_2 crystal was 1.15 at.%, and the concentration of Tm^{3+} ion in the Tm: PbF_2 crystal was 0.59 at.%.

The crystalline structure of as-grown samples was observed utilizing D/max2550 X-ray diffraction (XRD) with $\text{Cu K}\alpha$ radiation. The Perkin–Elmer UV-VIS-NIR spectrometer (Lambda 900) with a resolution of 1 nm was used to detect the absorption spectra of prepared samples in the range of 400–2200 nm. The emission spectra, up-conversion fluorescence spectra, and fluorescence decay curves were detected and recorded using the Edinburgh Instruments FLS920 and FSP920 spectrophotometers. The repetition frequency of the excitation pulse for measuring the fluorescence decay curves was set to 20 Hz, and the duration of the excitation pulses was 30s. All the measurements were performed at room temperature.

3. Calculation Method

In the framework of density functional theory, VASP codes and the plane-wave basis set method were used for calculation [38,39]. The mutual interactions were described by the projector augmented-wave pseudopotential with an exchange-correlation function (Perdew–Burke–Ernzerhof form) [40,41]. The cut-off was set at 550 eV and a $1 \times 1 \times 1$ Gamma k-grid was used to guarantee the relaxation accuracy of 10^{-5} eV and $0.01 \text{ eV}\text{\AA}^{-1}$ within a $2 \times 2 \times 2$ supercell, respectively. The spin polarization was included in the calculations. According to the method reported previously [42], the formation energy (ΔE) and cluster symbols were obtained. It is pointed that the energy correction of the PbF_2 crystal was different from that of CaF_2 , SrF_2 , and BaF_2 crystals. For a $2 \times 2 \times 2$ supercell with a net charge, the calculated value in PbF_2 crystal was 0.069 eV.

4. Results and Discussion

4.1. Crystal Structure Analysis

Figure 1 shows the XRD patterns and refined XRD patterns of the Er: PbF_2 , Tm: PbF_2 , Er/Tm: PbF_2 crystals, and the JCPDS standard card of the PbF_2 crystal (nos. 06-2051) [37]. The residuals of refinements (fit profiles shown in Figure 1) of Er: PbF_2 , Tm: PbF_2 , Er/Tm: PbF_2 crystals were 9.61%, 7.71%, 10.17%, respectively. It is obvious that no clear shift in the phase diffraction peaks was observed and all XRD curves were well matched with the standard card of the β - PbF_2 crystalline phase (nos. 06-2051). The results demonstrate successful co-doping of Er^{3+} and Tm^{3+} ions in PbF_2 crystal without phase transitions.

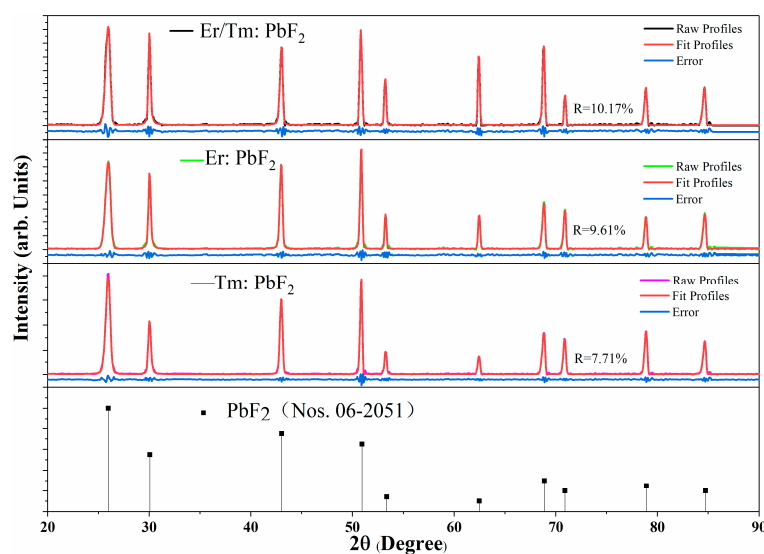


Figure 1. XRD patterns and refined XRD patterns of the Er/Tm: PbF_2 , Er: PbF_2 , Tm: PbF_2 crystals and PbF_2 crystal standard card.

4.2. First-Principles Calculations

Based on the first-principles calculations, the cluster structure of Tm^{3+} and Er^{3+} ions were simulated to research the change of local structures of doping ions in PbF_2 crystal. The possible thermodynamically stable Er^{3+} and Tm^{3+} centers in PbF_2 crystals are shown in Figure 2a,b. It is clear to see that there are 9 different types of centers in each $\text{Tm}:\text{PbF}_2$ and $\text{Er}:\text{PbF}_2$ crystals. In particular, only the $3_1|0|8|4_1\text{-C}$ center in the $\text{Tm}:\text{PbF}_2$ crystal varies from the $2_1|0|6|3_1$ center in the $\text{Er}:\text{PbF}_2$ crystal, and the other eight different types of centers in the $\text{Tm}:\text{PbF}_2$ crystal are the same as the $\text{Er}:\text{PbF}_2$ crystal. Moreover, Figure 2c shows the formation energy of Er^{3+} and Tm^{3+} versus the number of Er^{3+} and Tm^{3+} ions within a cluster, respectively. It can be seen that the slope of Er^{3+} clusters in PbF_2 crystal is -0.988 eV, which is almost the same as the slope of Tm^{3+} clusters in the PbF_2 crystal (-1.003 eV). These results indicate that the clustering characteristics of Er^{3+} and Tm^{3+} ions in PbF_2 crystal are almost consistent. This phenomenon agreed well with the approximately equal segregator coefficients of Er^{3+} (1.15) and Tm^{3+} (1.16) in the $\text{Er}/\text{Tm}:\text{PbF}_2$ crystal mentioned above, which may be owing to the slightly different ion radii between Er^{3+} (88.1 pm) and Tm^{3+} (86.9 pm) ions. That is to say, it can be considered that the Er^{3+} and Tm^{3+} ions replace Pb^{2+} ions with equal probability when they are co-doped in PbF_2 crystal, which makes the Er^{3+} and Tm^{3+} ions more evenly distributed in the PbF_2 crystal. The results suggest that the efficient energy transfer between Er^{3+} and Tm^{3+} ions can be guaranteed due to the uniform distribution of Er^{3+} and Tm^{3+} ions, and result in the enhancing of 2.78 μm MIR fluorescence emission in the ensuing discussion.

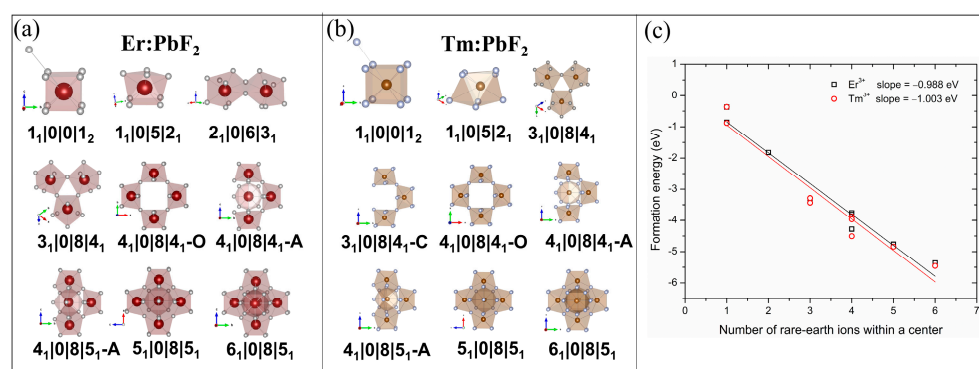


Figure 2. (a) Thermodynamically stable Er^{3+} centers in PbF_2 crystal; (b) Thermodynamically stable Tm^{3+} centers in PbF_2 crystal; (c) Formation energy of Er^{3+} and Tm^{3+} versus the number of rare-earth ions within a cluster.

4.3. Absorption Spectroscopy

The illustrations in Figure 3 shows the photos of $\text{Er}/\text{Tm}:\text{PbF}_2$, $\text{Er}:\text{PbF}_2$, $\text{Tm}:\text{PbF}_2$ crystals and their cut and polished crystal pieces; their sizes are also marked, respectively. It can be seen that all the crystal pieces are transparent and have no inclusions. Figure 3 illustrates the room temperature absorption spectra of $\text{Er}:\text{PbF}_2$, $\text{Tm}:\text{PbF}_2$, and $\text{Er}/\text{Tm}:\text{PbF}_2$ crystals ranging from 400 nm to 2200 nm. Clearly, the typical absorption bands centered at approximately 417 , 451 , 486 , 521 , 541 , 650 , 802 , 975 , and 1509 nm in the $\text{Er}:\text{PbF}_2$ crystal originated from the transitions from the ground state $4I_{15/2}$ level to upper-lying $2H_{9/2}$, $4F_{5/2,3/2}$, $4F_{7/2}$, $2H_{11/2}$, $4S_{3/2}$, $4F_{9/2}$, $4I_{9/2}$, $4I_{11/2}$ and $4I_{13/2}$ levels of Er^{3+} ion, respectively [37]. While in the $\text{Tm}:\text{PbF}_2$ crystal mainly five absorption bands of Tm^{3+} ion are labeled, the absorption peaks centered at round 464 , 680 , 792 , 1211 , and 1618 nm are in accord with the transitions from ground state $3H_6$ level to upper-lying $1G_4$, $3F_{2,3}$, $3H_4$, $3H_5$ and $3F_4$ levels, respectively. Obviously, the huge absorption band centered at around 792 nm in the range of 750 – 830 nm corresponding to $\text{Tm}^{3+}: 3H_6 \rightarrow 3H_4$ transition well coincides with the wavelength of 808 nm AlGaAs LD pumping. The absorption bands in the $\text{Er}/\text{Tm}:\text{PbF}_2$ crystal are altogether composed of the transitions of Er^{3+} and Tm^{3+} ions discussed above, indicating the successful introduction of both Er^{3+} and Tm^{3+}

ions. Strong overlap between the $\text{Tm}^{3+}: {}^3\text{H}_6 \rightarrow {}^3\text{H}_4$ absorption transition and the $\text{Er}^{3+}: {}^4\text{I}_{15/2} \rightarrow {}^4\text{I}_{9/2}$ absorption transition can be seen in the Er/Tm: PbF_2 crystal. The absorption overlap indicates that a possible nonradiative energy transfer process $\text{Tm}^{3+}: {}^3\text{H}_4 \rightarrow \text{Er}^{3+}: {}^4\text{I}_{9/2}$ would effectively occur for enhancing the absorption efficiency of Er^{3+} ion ~ 800 nm. Therefore, benefiting from the broad absorption band of Tm^{3+} ion centered at around LD pump wavelength and the possibility for energy transfer, the Tm^{3+} ion can act as a suitable sensitizer for Er^{3+} ion in the Er/Tm dual-doped PbF_2 crystal.

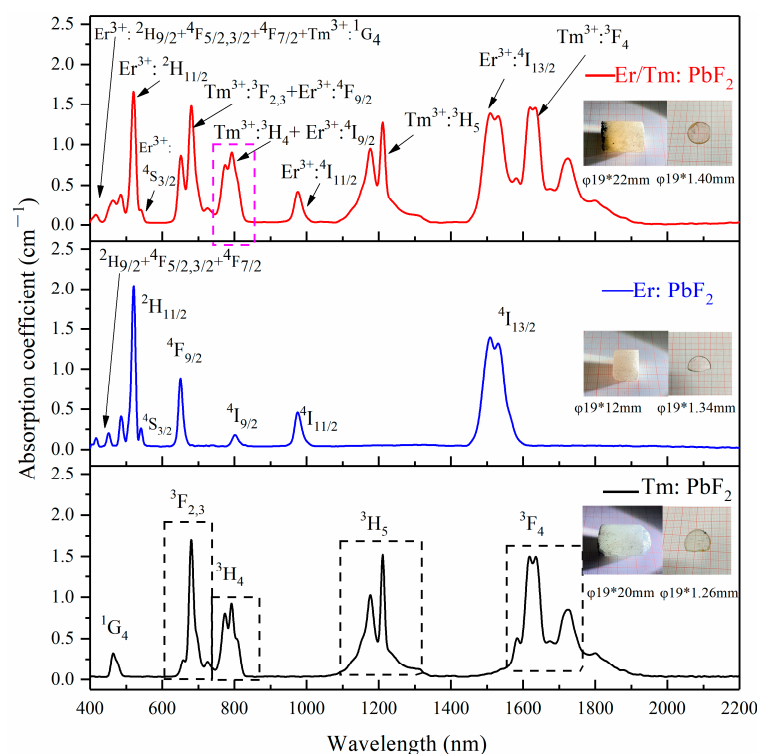


Figure 3. Absorption spectra of Tm: PbF_2 , Er: PbF_2 , and Er/Tm: PbF_2 crystals ranging from 400 to 2200 nm at room temperature. (Illustration: the photos of Er/Tm: PbF_2 , Er: PbF_2 , Tm: PbF_2 crystals and their cut and polished crystal pieces, respectively.)

For demonstrating the sensitization effect of Tm^{3+} ion for Er^{3+} ion via the $\text{Tm}^{3+}: {}^3\text{H}_4 \rightarrow \text{Er}^{3+}: {}^4\text{I}_{9/2}$ energy transfer transition, the lifetimes of $\text{Tm}^{3+}: {}^3\text{H}_4$ level in the Tm^{3+} single-doped and Er/Tm dual-doped PbF_2 crystals were measured and shown in Figure 4a,b, respectively. The decay curves were measured under the condition of $1.47 \mu\text{m}$ emission ($\text{Tm}^{3+}: {}^3\text{H}_4 \rightarrow {}^3\text{F}_4$) and 800 nm excitation ($\text{Tm}^{3+}: {}^3\text{H}_6 \rightarrow {}^3\text{H}_4$) and were all well fitted by single-exponential behavior. As shown in Figure 4a, the measured lifetime of the $\text{Tm}^{3+}: {}^3\text{H}_4$ manifold is 1.67 ms in the Tm: PbF_2 crystal, while the lifetime is 0.54 ms in the Er/Tm: PbF_2 crystal shown in Figure 4b. The remarkable decreasing lifetime in the Er/Tm: PbF_2 crystal indicates the effective sensitization effect of the Tm^{3+} ion. The energy transfer efficiency from $\text{Tm}^{3+}: {}^3\text{H}_4$ to $\text{Er}^{3+}: {}^4\text{I}_{9/2}$ level can be calculated by the following equation: $\eta_{ET1} = 1 - \tau_{\text{Er/Tm}} / \tau_{\text{Tm}}$, where $\tau_{\text{Er/Tm}}$ and τ_{Tm} are the lifetimes of $\text{Tm}^{3+}: {}^3\text{H}_4$ level in Tm: PbF_2 , Er/Tm: PbF_2 crystals, respectively. The high value of η_{ET1} (67.66%) confirms that the Tm^{3+} ion has a significant influence on $\text{Er}^{3+}: {}^4\text{I}_{9/2}$ level in PbF_2 crystal, and can effectively act as a sensitizer for Er^{3+} ion for enhancing $\sim 2.7 \mu\text{m}$ MIR emission.

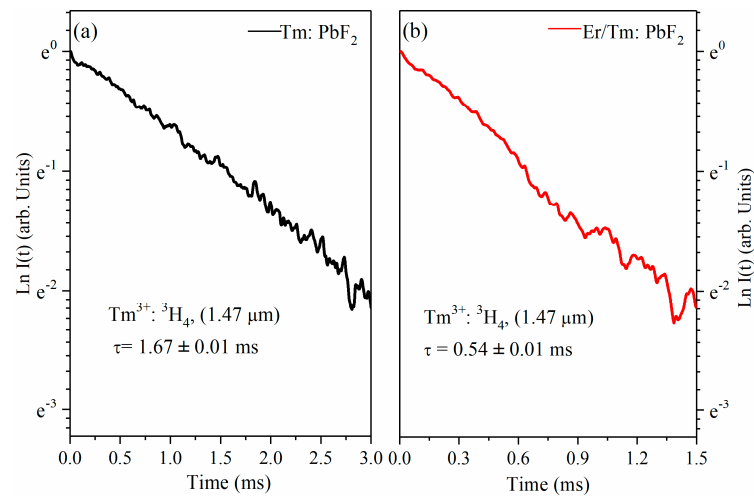


Figure 4. (a) Fluorescence decay curves of the $\text{Tm}^{3+}: {}^3\text{H}_4$ energy level of Tm: PbF_2 crystal; (b) fluorescence decay curves of the $\text{Tm}^{3+}: {}^3\text{H}_4$ energy level of Er/Tm: PbF_2 crystal ($\lambda_{\text{ex}} = 800 \text{ nm}$, $\lambda_{\text{em}} = 1470 \text{ nm}$).

4.4. Emission Spectra and Emission Cross-Sections

For further clarifying the energy transfer mechanism between Tm^{3+} and Er^{3+} ions, the emission spectra of Er/Tm: PbF_2 , Er: PbF_2 samples in the range of 1400–1700 nm, and Er/Tm: PbF_2 , Tm: PbF_2 samples in the 1700–2200 nm region are shown in Figure 5a,b, respectively. The test parameters of the luminescence performance of the prepared samples, such as pump power and slits, are uniformed. As shown in Figure 5a, compared with the Er: PbF_2 crystal the emission intensity centered at around 1.55 μm corresponding to the $\text{Er}^{3+}: {}^4\text{I}_{13/2} \rightarrow {}^4\text{I}_{15/2}$ transition in the Er/Tm: PbF_2 crystal weakened sharply, at almost ten times lower. The result shows that the introduction of Tm^{3+} ion would significantly reduce the population of the $\text{Er}^{3+}: {}^4\text{I}_{13/2}$ energy level, thereby enhancing the $\sim 2.7 \mu\text{m}$ mid-infrared emission and reversely weakening the 1.55 μm infrared emission. This depopulation of $\text{Er}^{3+}: {}^4\text{I}_{13/2}$ energy level is mainly attributed to the deactivation effect of Tm^{3+} ions via energy transfer process: $\text{Er}^{3+}: {}^4\text{I}_{13/2} \rightarrow \text{Tm}^{3+}: {}^3\text{F}_4$ in Er/Tm: PbF_2 crystal. As the deactivation energy transfer process occurs, the population on the $\text{Tm}^{3+}: {}^3\text{F}_4$ level would increase, thereby enhancing the 1.91 μm emission ($\text{Tm}^{3+}: {}^3\text{F}_4 \rightarrow {}^3\text{H}_6$ transition) in the Er/Tm: PbF_2 crystal, but it is actually weakened (shown in Figure 5b). The 1.91 μm emission intensity of the Tm^{3+} ion in Er/Tm: PbF_2 crystal is nearly three times lower than that in the Tm^{3+} single doped PbF_2 crystal. This result is mainly assigned to the cross-relaxation (CR) process between Tm^{3+} and Er^{3+} ions ($\text{Tm}^{3+}: {}^3\text{F}_4 + \text{Er}^{3+}: {}^4\text{I}_{13/2} \rightarrow \text{Tm}^{3+}: {}^3\text{H}_4 + \text{Er}^{3+}: {}^4\text{I}_{15/2}$), bringing about the depopulation of the $\text{Tm}^{3+}: {}^3\text{F}_4$ level and $\text{Er}^{3+}: {}^4\text{I}_{13/2}$ level. Therefore, the reduced emission intensity of 1.55 μm of Er^{3+} ion and 1.91 μm of Tm^{3+} ion both would depopulate the ions on the $\text{Er}^{3+}: {}^4\text{I}_{13/2}$ level, which is beneficial to enhance $\sim 2.7 \mu\text{m}$ MIR emission. More importantly, as shown in Figure 6, the emission intensity of the Er/Tm: PbF_2 crystal centered at around 2.7 μm in the 2500–3100 nm region is remarkably larger than that of the Er: PbF_2 crystal, confirming that the efficient enhanced $\sim 2.7 \mu\text{m}$ emission is achieved in the Er/Tm: PbF_2 designed crystal. To further confirm the prospects of Er: PbF_2 , Er/Tm: PbF_2 crystals as the mid-infrared luminescent material in laser applications, the 2.78 μm emission cross-sections are subsequently calculated according to the Fuchtbauere–Ladenburg theory [43]:

$$\sigma_{\text{em}}(\lambda) = \frac{A\beta\lambda^5 I(\lambda)}{8\pi cn^2 \int \lambda I(\lambda) d\lambda} \quad (1)$$

where λ denotes the wavelength of fluorescence spectrum, $I(\lambda)$ is the intensity of emission spectrum at λ , $I(\lambda)/\int \lambda I(\lambda) d\lambda$ is the normalized line shape function of the emission spectrum of prepared crystal, n is the refractive index of PbF_2 crystal, c is the speed of light in a vacuum, β is the fluorescence branching ratio of ${}^4\text{I}_{11/2} \rightarrow {}^4\text{I}_{13/2}$ transition, and A is

the spontaneous emission probability. The value of β for $\sim 2.7 \mu\text{m}$ mid-infrared emission in Er: PbF₂ is calculated to be 14.9%, and in the Er/Tm: PbF₂ crystal is calculated to be 20.24%. The maximum emission cross-section of the Er/Tm: PbF₂ crystal is calculated to be $0.63 \times 10^{-20} \text{ cm}^2$ at 2780 nm, which is almost twice that of the Er: PbF₂ crystal ($0.32 \times 10^{-20} \text{ cm}^2$). Moreover, as shown in Table 1, this higher stimulated emission cross-section in the Er/Tm: PbF₂ crystal possibly coincides well with the higher fluorescence branching ratio β (20.24%) of the Er³⁺: $^4I_{11/2} \rightarrow ^4I_{13/2}$ transition. A higher emission cross-section is more favorable in achieving high performance of MIR laser operation. These results are related to the more uniform distribution of Er³⁺ and Tm³⁺ ions in PbF₂ crystal after the co-doping of Tm³⁺ ions, which is consistent with the theoretical calculation results. Furthermore, it is pointed out that the enhancing of 2.78 μm MIR fluorescence emission is more dependent on the efficient energy transfer between Er³⁺ and Tm³⁺ ions, which comes from the uniform distribution of doped ions.

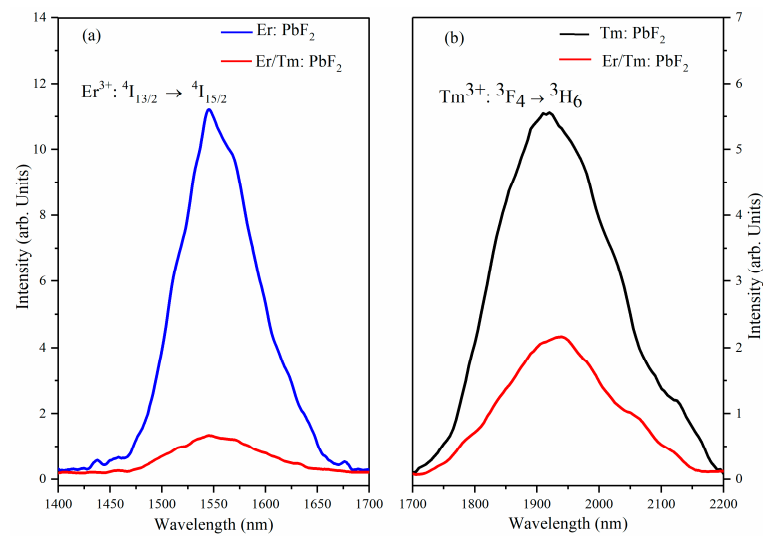


Figure 5. (a) Emission spectra of the Er: PbF₂, Er/Tm: PbF₂ crystals in the range of 1400–1700 nm ($\lambda_{\text{ex}} = 800\text{nm}$); (b) emission spectra of Tm: PbF₂, Er/Tm: PbF₂ crystals in the range of 1700–2200 nm ($\lambda_{\text{ex}} = 800\text{nm}$).

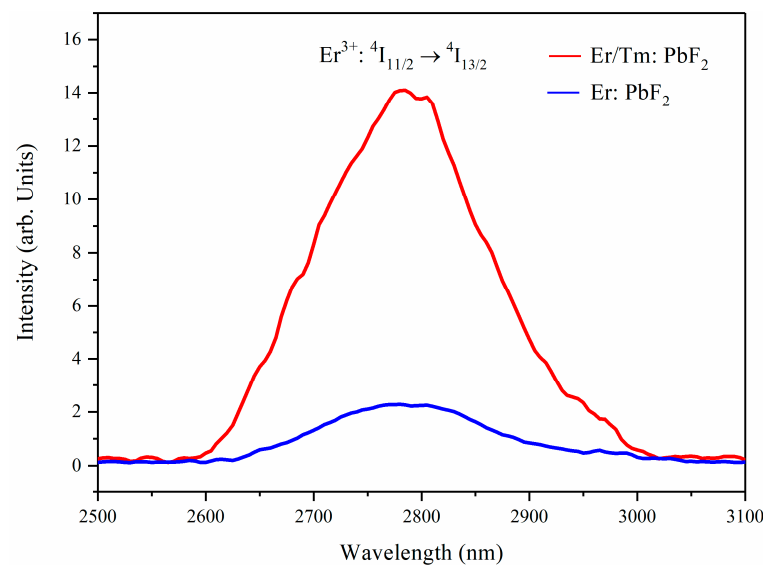


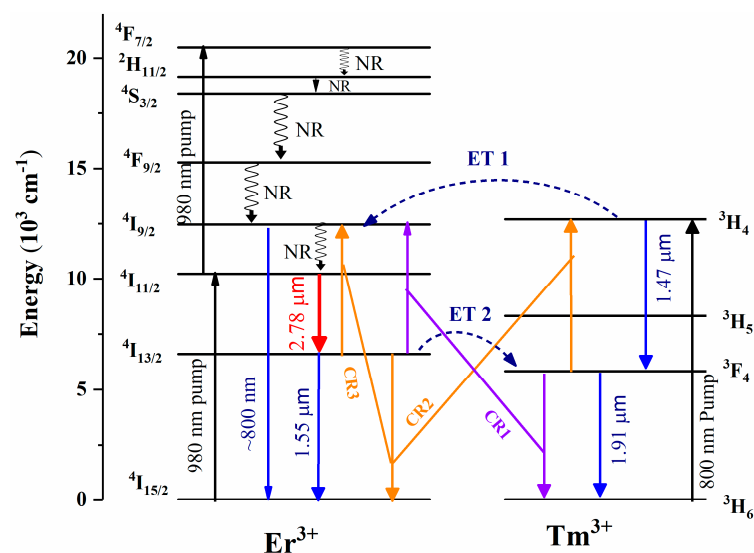
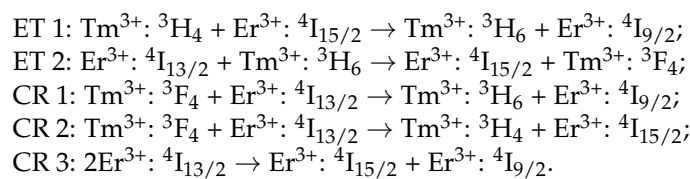
Figure 6. Emission spectra of the Er: PbF₂, Er/Tm: PbF₂ crystals in the range of 2500–3100 nm ($\lambda_{\text{ex}} = 800 \text{ nm}$).

Table 1. MIR emission cross-sections σ_{em} , and lifetimes of ${}^4I_{11/2}$, ${}^4I_{13/2}$ levels of Er/Tm: PbF₂, Er: PbF₂ crystals compared with other Er³⁺-doped crystals.

Crystal	σ_{em} (10 ⁻²⁰ cm ²)	$\tau({}^4I_{11/2})$ (ms)	$\tau({}^4I_{13/2})$ (ms)	$\tau({}^4I_{11/2})/\tau({}^4I_{13/2})$ (%)	Ref.
1.0 at.% /0.5 at.% Er/Tm: PbF ₂	0.63@2780nm	6.91 ± 0.01	3.14 ± 0.01	220.06	[This work]
1 at.% Er: PbF ₂	0.32@2780nm	6.03 ± 0.01	12.06 ± 0.05	50.00	[This work]
10 at.% Er:BaLaGa ₃ O ₇	7.34@2714nm	0.72	7.99	9.01	[44]
10 at.% Er:CaLaGa ₃ O ₇	17.9@2702nm	0.77	8.41	9.16	[45]
8 at.%Er:LuAl ₃ (BO ₃) ₄	8.60@3170nm	2.10	2.54	82.68	[46]
7 at.% Er:Y ₂ O ₃	1.41@2723nm	2.95	17.57	16.79	[47]
10 at.% Er:SrGdGa ₃ O ₇	1.30@2.7μm	1.10	4.48	24.55	[24]
5at.% Er:YAP	9.00@2792nm	0.85	7.30	11.64	[13]
7 at.% Er:Lu ₂ O ₃	1.10@2730nm	1.10	4.30	25.58	[14]
5 at.% Er:GdScO ₃	0.93@2720nm	2.24	4.57	49.02	[15]
4 at.% Er:SrF ₂	0.78@2727nm	9.56	15.06	63.48	[16]
4 at.% Er:CaF ₂	0.65@2720nm	5.98	9.94	60.16	[16]

4.5. Energy Transfer Mechanism between Tm³⁺ and Er³⁺ Ions

Based on spectroscopic results discussed above, the simplified energy level scheme and electron transitions of the Er³⁺/Tm³⁺ co-doped PbF₂ crystal are presented in Figure 7. The cyclic related processes of the Tm³⁺ and Er³⁺ ions in the crystal under optical excitation are as follows: cross-relaxation, energy transfer between Tm³⁺ and Er³⁺ ions, and multiphonon relaxation. The main two ET (namely ET1, ET2) and three CR (namely CR1, CR2, CR3) processes are listed as follows:

**Figure 7.** Simplified energy level scheme and electron transitions of Er³⁺/Tm³⁺ co-doped system.

As discussed, the Tm³⁺: ${}^3\text{H}_4 \rightarrow {}^3\text{H}_6$ transition is resonant with the Er³⁺: ${}^4\text{I}_{15/2} \rightarrow {}^4\text{I}_{9/2}$ transition in the Er/Tm: PbF₂ crystal. Therefore, after the crystal is excited to the Tm³⁺: ${}^3\text{H}_4$ level by a pump of 800 nm LD, ET1 process Tm³⁺: ${}^3\text{H}_4 \rightarrow \text{Er}^{3+}: {}^4\text{I}_{9/2}$ would occur. Ions in the Er³⁺: ${}^4\text{I}_{9/2}$ level decay non-radiatively to the lower Er³⁺: ${}^4\text{I}_{11/2}$ level, and then decay radiatively to the Er³⁺: ${}^4\text{I}_{13/2}$ level and emit 2.78 μm mid-infrared light. Ions in the Er³⁺:

$^4I_{13/2}$ level continue to decay radiatively to the ground state Er^{3+} : $^4I_{15/2}$ level and emit 1.55 μm infrared light. Similarly, the Er^{3+} : $^4I_{13/2} \rightarrow ^4I_{15/2}$ transition is resonant with the Tm^{3+} : $^3H_6 \rightarrow ^3F_4$ transition, and the ET2 process from Er^{3+} : $^4I_{13/2}$ to Tm^{3+} : 3F_4 level takes place. The ET2 process would reduce the population of the lower level of Er^{3+} : $^4I_{13/2}$, thereby enhancing the 2.78 μm emission and weakening the 1.55 μm emission, as shown in Figures 5a and 6. Meantime, the energy transfer up-conversion (UC) CR3 process (Er^{3+} : $2^4I_{13/2} \rightarrow ^4I_{15/2} + ^4I_{9/2}$) in the crystal can also populate the Er^{3+} : $^4I_{11/2}$ level and depopulate the Er^{3+} : $^4I_{13/2}$ level. Additionally, ions in the Tm^{3+} : 3F_4 level decay radiatively to the 3H_6 level and emit 1.91 μm emission. The subsequent CR1 populates the Er^{3+} : $^4I_{9/2}$ level, and then the Er^{3+} : $^4I_{11/2}$ level is populated through the nonradiative decay from the $^4I_{9/2}$ level to the $^4I_{11/2}$ level, increasing the population ratio of $^4I_{11/2}/^4I_{13/2}$ levels. Moreover, the ions in the Tm^{3+} : 3F_4 energy level will also absorb energy and jump to the upper Tm^{3+} : 3H_4 energy level due to Stark level splitting, and then the CR2 process described above occurs. The CR2 process can simultaneously reduce the population Er^{3+} : $^4I_{13/2}$, Tm^{3+} : 3F_4 levels, to achieve 2.78 μm emission enhancement and 1.91 μm emission reduction, as shown in Figures 5b and 6. The CR2 process also brings about the increasing population of the Tm^{3+} : 3H_4 level. Besides emitting 1.47 μm light via the Tm^{3+} : $^3H_4 \rightarrow ^3F_4$ transition, ions in the Tm^{3+} : 3H_4 level can populate the Er^{3+} : $^4I_{9/2}$ level via ET1 process, resulting in further enhancement of the sensitization effect. To prove the CR2 process, the UC emission spectra of Er: PbF₂ and Er/Tm: PbF₂ crystals are shown in Figure 8 under 980 nm excitation. Clearly, as shown in Figure 7, under 980 nm NIR light excitation, the electrons in the ground level $^4I_{15/2}$ can be excited to the intermediate level $^4I_{11/2}$, and the electrons in the $^4I_{11/2}$ level sequentially populate the $^4F_{7/2}$ level ($^4I_{15/2} \rightarrow ^4I_{11/2} \rightarrow ^4F_{7/2}$). Additionally, then, the multiple nonradiative multi-phonon relaxation in the $^4F_{7/2}$ state in turn populate the lower $^2H_{11/2}$, $^4S_{3/2}$, $^4F_{9/2}$, and $^4I_{9/2}$ levels, which would produce 800 nm light via the process: $^4I_{9/2} \rightarrow ^4I_{15/2}$. It is clear to see that the UC emission intensity of the Er/Tm: PbF₂ crystal is at least two times larger than that of the Er: PbF₂ crystal at around 800 nm. Obviously, Tm^{3+} ions have no absorption band matching the 980 nm excitation (shown in Figure 3). This enhancing UC emissions phenomenon is possibly assigned to the CR2 and ET1 mechanism processes illustrated in Figure 7. To summarize, the ET1, ET2, CR1, CR2, CR3 processes all have significant effects on narrowing the lifetime gap of upper-lying Er^{3+} : $^4I_{11/2}$ and lower-lying Er^{3+} : $^4I_{13/2}$ levels or even achieving population conversion of these two levels, thereby obtaining efficient enhanced 2.78 μm emission.

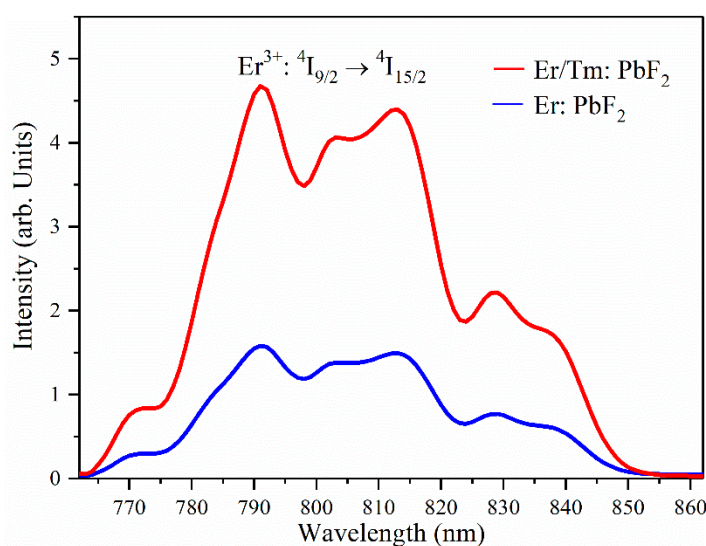


Figure 8. Up-conversion emissions of Er: PbF₂, and Er/Tm: PbF₂ crystals in the range of 760–860 nm ($\lambda_{\text{ex}} = 980\text{nm}$).

4.6. Fluorescence Decay Curves and Fluorescence Lifetimes

For further demonstrating the energy interaction mechanism between Er^{3+} and Tm^{3+} ions, the time-resolved decay curves of the Er^{3+} ion $2.78 \mu\text{m}$ (${}^4\text{I}_{11/2} \rightarrow {}^4\text{I}_{13/2}$) and $1.55 \mu\text{m}$ (${}^4\text{I}_{13/2} \rightarrow {}^4\text{I}_{15/2}$) fluorescence emission for the Er/Tm: PbF_2 and Er: PbF_2 crystals were measured and shown in Figure 9. The lifetimes of ${}^4\text{I}_{13/2}$ levels were measured under the conditions of $1.55 \mu\text{m}$ emission (${}^4\text{I}_{13/2} \rightarrow {}^4\text{I}_{15/2}$) and $1.49 \mu\text{m}$ excitation (${}^4\text{I}_{15/2} \rightarrow {}^4\text{I}_{13/2}$). The decay curves of the Er^{3+} : ${}^4\text{I}_{11/2}$ and Er^{3+} : ${}^4\text{I}_{13/2}$ levels are well fitted with single-exponential behavior. As shown in Figure 9a,b, the measured lifetime of the upper-lying ${}^4\text{I}_{11/2}$ level in the Er/Tm: PbF_2 crystal (6.91 ms) is 14.6% longer compared with the Er: PbF_2 crystal (6.03 ms), which is assigned to the sensitization effect of the Tm^{3+} ion on the upper-lying Er^{3+} : ${}^4\text{I}_{11/2}$ level. Moreover, as shown in Figure 9c,d, the measured lifetime of the lower-lying ${}^4\text{I}_{13/2}$ level in the Er/Tm: PbF_2 crystal is 3.14 ms, which is 73.96% shorter compared with the Er: PbF_2 crystal (12.06 ms). This remarkable decrease of the lifetime of lower-lying ${}^4\text{I}_{13/2}$ level denotes that Tm^{3+} ions can dramatically depopulate the Er^{3+} : ${}^4\text{I}_{13/2}$ level via ET2, CR1, CR2, CR3 processes, thereby enhancing the $2.78 \mu\text{m}$ emission in PbF_2 crystals. The ET2, CR1, CR2, CR3 processes all have significant effects on narrowing the lifetime gap of upper-lying Er^{3+} : ${}^4\text{I}_{11/2}$ and lower-lying Er^{3+} : ${}^4\text{I}_{13/2}$ levels or even achieving population conversion of these two levels. Besides, the energy transfer efficiency η_{ET2} was calculated to be 73.96%, confirming the efficient deactivation effect of the Tm^{3+} ion for the Er^{3+} ion. Furthermore, Table 1 shows the lifetimes of ${}^4\text{I}_{11/2}$, ${}^4\text{I}_{13/2}$ levels of Er/Tm: PbF_2 , Er: PbF_2 crystals, and other Er^{3+} doped laser crystals. The shorter fluorescence lifetime of ${}^4\text{I}_{13/2}$ lower level induces the longer fluorescence lifetime ratio $\tau({}^4\text{I}_{11/2})/\tau({}^4\text{I}_{13/2})$. The fluorescence lifetime ratio $\tau({}^4\text{I}_{11/2})/\tau({}^4\text{I}_{13/2})$ in Er/Tm: PbF_2 crystal is 220.06%, which is dramatically larger than that of the Er: PbF_2 crystal (50.00%) and other Er^{3+} doped crystals. The remarkably enhanced $\tau({}^4\text{I}_{11/2})/\tau({}^4\text{I}_{13/2})$ ratio in Er/Tm: PbF_2 crystal is favorable for achieving efficient laser operation $\sim 2.7 \mu\text{m}$. As a consequence, the introduction of Tm^{3+} ions can simultaneously act as sensitization and deactivation ions for the Er^{3+} ion, thereby enhancing $2.78 \mu\text{m}$ mid-infrared emission and reducing the laser threshold of $2.78 \mu\text{m}$ luminescence.

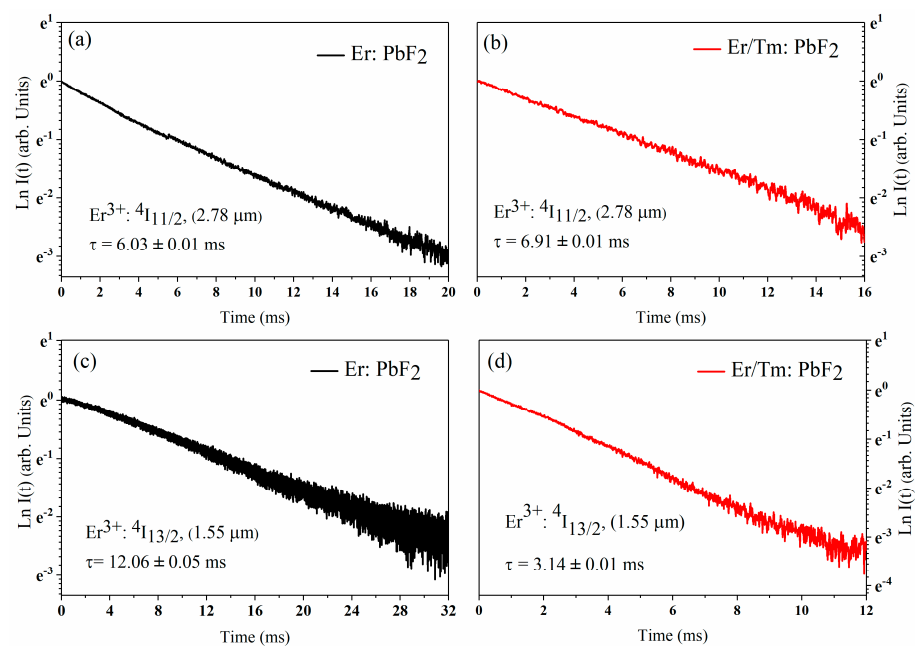


Figure 9. (a) Fluorescence decay curves of the Er^{3+} : ${}^4\text{I}_{11/2}$ energy level of Er: PbF_2 crystal ($\lambda_{\text{ex}} = 800 \text{ nm}$, $\lambda_{\text{em}} = 2780 \text{ nm}$); (b) Er^{3+} : ${}^4\text{I}_{11/2}$ energy level of Er/Tm: PbF_2 crystal ($\lambda_{\text{ex}} = 800 \text{ nm}$, $\lambda_{\text{em}} = 2780 \text{ nm}$); (c) Er^{3+} : ${}^4\text{I}_{13/2}$ energy level of Er: PbF_2 crystal ($\lambda_{\text{ex}} = 1490 \text{ nm}$, $\lambda_{\text{em}} = 1550 \text{ nm}$); (d) Er^{3+} : ${}^4\text{I}_{13/2}$ energy level of Er/Tm: PbF_2 crystal ($\lambda_{\text{ex}} = 1490 \text{ nm}$, $\lambda_{\text{em}} = 1550 \text{ nm}$).

5. Conclusions

In summary, $\text{Er}^{3+}:\text{PbF}_2$, $\text{Tm}^{3+}:\text{PbF}_2$, and $\text{Er}^{3+}/\text{Tm}^{3+}:\text{PbF}_2$ crystals were prepared successfully by the Bridgman technique. An efficient enhanced 2.78 μm emission was obtained in the $\text{Er}/\text{Tm}:\text{PbF}_2$ crystal for the first time, and the proposed energy transfer mechanism of the $\text{Er}/\text{Tm}:\text{PbF}_2$ crystal was systematically investigated. The theoretical calculations were performed to discover that the co-doping of Tm^{3+} ions can make the Er^{3+} and Tm^{3+} ions more evenly distributed in PbF_2 crystals, which can effectively break the local clusters of Er^{3+} in $\text{Er}:\text{PbF}_2$ crystal, thus ensuring efficient energy transfer between Er^{3+} and Tm^{3+} ions, and resulting in the enhancing of 2.78 μm MIR fluorescence emission. The cyclic energy transfer mechanism contains several energy transfer processes and cross-relaxation processes, which all have significant effects on narrowing the lifetime gap of upper-lying $\text{Er}^{3+}:\ ^4\text{I}_{11/2}$ and lower-lying $\text{Er}^{3+}:\ ^4\text{I}_{13/2}$ levels or even achieving population conversion of these two levels. As proved, the Tm^{3+} ion can simultaneously act as an appropriate sensitized and deactivated ion for the Er^{3+} ion in the PbF_2 crystal. Compared with the Er^{3+} single-doped crystal, the $\text{Er}^{3+}/\text{Tm}^{3+}$ co-doped PbF_2 crystal has the larger 2.78 μm mid-infrared fluorescence emission intensity, higher fluorescence branching ratio (20.24%), and higher stimulated emission cross-section ($0.63 \times 10^{-20} \text{ cm}^2$), corresponding to $\text{Er}^{3+}:\ ^4\text{I}_{11/2} \rightarrow ^4\text{I}_{13/2}$ transition. Therefore, the introduction of Tm^{3+} ions is favorable for achieving efficient enhanced 2.78 μm emission in the $\text{Er}/\text{Tm}:\text{PbF}_2$ crystal, which can become a promising material for low threshold, and high-efficiency mid-infrared laser applications under the pump of a conventional 800 nm LD.

Author Contributions: Conceptualization, P.Z.; methodology, J.L. and Q.C.; software, F.M.; validation, Y.H.; formal analysis, S.Z.; investigation, J.L., H.T. and Q.Y.; resources, Y.H.; and Z.L.; data curation, J.L. and Q.C.; writing—original draft preparation, J.L. and X.N.; writing—review and editing, P.Z.; visualization, Q.C.; supervision, Z.C.; project administration, Z.C.; funding acquisition, Y.H. and Z.L. All authors have read and agreed to the published version of the manuscript.

Funding: This work was supported by the National Natural Science Foundation of China (NSFC) (51972149, 51872307, 61935010, 51702124); Key-Area Research and Development Program of Guangdong Province (2020B090922006); Guangdong Project of Science and Technology Grants (2018B030323017, 2018B010114002); Guangzhou science and technology project (201904010385, 201903010042); The Fundamental Research Funds for the Central Universities (21620445).

Institutional Review Board Statement: Not applicable.

Informed Consent Statement: Not applicable.

Data Availability Statement: The data presented in this study are available on request from the corresponding author.

Conflicts of Interest: The authors declare no conflict of interest.

References

1. Popov, A.; Sherstnev, V.; Yakovlev, Y.P.; Baranov, A.; Alibert, C. Powerful Mid-Infrared Light Emitting Diodes for Pollution Monitoring. *Electron. Lett.* **1997**, *33*, 86–88. [[CrossRef](#)]
2. Bekman, H.T.; Van Den Heuvel, J.; Van Putten, F.; Schleijsen, R. Development of a Mid-Infrared Laser for Study of Infrared Countermeasures Techniques. In Proceedings of the Technologies for Optical Countermeasures, London, UK, 26–27 October 2004; Volume 5615, pp. 27–38.
3. Hu, T.; Dong, B.; Luo, X.; Liow, T.Y.; Song, J.; Lee, C.; Lo, G.Q. Silicon Photonic Platforms for Mid-Infrared Applications. *Photonics Res.* **2017**, *5*, 417–430. [[CrossRef](#)]
4. Walsh, B.M.; Lee, H.R.; Barnes, N.P. Mid Infrared Lasers for Remote Sensing Applications. *J. Lumin.* **2016**, *169*, 400–405. [[CrossRef](#)]
5. Urich, A.; Maier, R.R.J.; Yu, F.; Knight, J.C.; Hand, D.P. Silica Hollow Core Microstructured Fibres for Mid-Infrared Surgical Applications. *J. Non-Cryst. Solids* **2013**, *377*, 236–239. [[CrossRef](#)]
6. Godard, A. Infrared (2–12 Mm) Solid-State Laser Sources: A Review. *Comptes Rendus Phys.* **2007**, *8*, 1100–1128. [[CrossRef](#)]
7. Vodopyanov, K.; Ganikhanov, F.; Maffetone, J.; Zwieback, I.; Ruderman, W. ZnGeP₂ Optical Parametric Oscillator with 3.8–12.4- μm Tunability. *Opt. Lett.* **2000**, *25*, 841–843. [[CrossRef](#)]
8. Zhang, T.; Feng, G.; Zhang, H.; Yang, X.; Dai, S.; Zhou, S. 2.78 μm Passively Q-Switched Er^{3+} -Doped Zblan Fiber Laser Based on PLD-Fe²⁺: Znse Film. *Laser Phys. Lett.* **2016**, *13*, 075102. [[CrossRef](#)]

9. Zhang, C.; Hao, Q.; Zu, Y.; Zong, M.; Guo, J.; Zhang, F.; Ge, Y.; Liu, J. Graphdiyne Saturable Absorber for Passively Q-Switched Ho³⁺-Doped Laser. *Nanomaterials* **2020**, *10*, 1848. [[CrossRef](#)]
10. Pajewski, L.; Sójka, L.; Lamrini, S.; Benson, T.M.; Seddon, A.B.; Sujecki, S. Gain-Switched Dy³⁺: Zblan Fiber Laser Operating around 3 μm. *J. Phys. Photonics* **2019**, *2*, 014003. [[CrossRef](#)]
11. Wu, Z.; Sun, D.; Wang, S.; Luo, J.; Li, X.; Huang, L.; Hu, A.; Tang, Y.; Guo, Q. Performance of a 967 nm Cw Diode End-Pumped Er: GSGG Laser at 2.79 μm. *Laser Phys.* **2013**, *23*, 055801. [[CrossRef](#)]
12. Arbabzadah, E.; Chard, S.; Amrania, H.; Phillips, C.; Damzen, M. Comparison of a Diode Pumped Er: YSGG and Er: YAG Laser in the Bounce Geometry at the 3 μm Transition. *Opt. Express* **2011**, *19*, 25860–25865. [[CrossRef](#)]
13. Kawase, H.; Yasuhara, R. 2.92-μm High-Efficiency Continuous-Wave Laser Operation of Diode-Pumped Er: YAP Crystal at Room Temperature. *Opt. Express* **2019**, *27*, 12213–12220. [[CrossRef](#)]
14. Li, T.; Beil, K.; Kränkel, C.; Huber, G. Efficient High-Power Continuous Wave Er: Lu₂O₃ Laser at 2.85 μm. *Opt. Lett.* **2012**, *37*, 2568–2570. [[CrossRef](#)] [[PubMed](#)]
15. Hou, W.; Zhao, H.; Qin, Z.; Liu, J.; Wang, D.; Xue, Y.; Wang, Q.; Xie, G.; Xu, X.; Xu, J. Spectroscopic and Continuous-Wave Laser Properties of Er: GdScO₃ Crystal at 2.7 μm. *Opt. Mater. Express* **2020**, *10*, 2730–2737. [[CrossRef](#)]
16. Ma, W.; Qian, X.; Wang, J.; Liu, J.; Fan, X.; Liu, J.; Su, L.; Xu, J. Highly Efficient Dual-Wavelength Mid-Infrared Cw Laser in Diode End-Pumped Er: SrF₂ Single Crystals. *Sci. Rep.* **2016**, *6*, 1–7.
17. Bandiello, E.; Sánchez-Martín, J.; Errandonea, D.; Bettinelli, M. Pressure effects on the optical properties of NdVO₄. *Crystals* **2019**, *9*, 237. [[CrossRef](#)]
18. Botella, P.; Enrichi, F.; Vomiero, A.; Muñoz-Santiuste, J.E.; Garg, A.B.; Arvind, A.; Manjón, F.J.; Segura, A.; Errandonea, D. Investigation on the Luminescence Properties of InMO₄ (M = V⁵⁺, Nb⁵⁺, Ta⁵⁺) Crystals Doped with Tb³⁺ or Yb³⁺ Rare Earth Ions. *ACS Omega* **2020**, *5*, 2148–2158. [[CrossRef](#)] [[PubMed](#)]
19. Zhang, P.; Chen, Z.; Hang, Y.; Li, Z.; Yin, H.; Zhu, S.; Fu, S.; Li, A. Enhanced 2.7 μm Mid-Infrared Emissions of Er³⁺ Via Pr³⁺ Deactivation and Yb³⁺ Sensitization in LiNbO₃ Crystal. *Opt. Express* **2016**, *24*, 25202–25210. [[CrossRef](#)]
20. Li, S.; Zhang, L.; Zhang, P.; Hang, Y. Nd³⁺ as Effective Sensitization and Deactivation Ions in Nd, Er: LaF₃ Crystal for the 2.7 μm Lasers. *J. Alloy. Compd.* **2020**, *827*, 154268. [[CrossRef](#)]
21. Li, M.; Liu, X.; Guo, Y.; Hao, W.; Hu, L.; Zhang, J. ~2 μm Fluorescence Radiative Dynamics and Energy Transfer between Er³⁺ and Tm³⁺ Ions in Silicate Glass. *Mater. Res. Bull.* **2014**, *51*, 263–270. [[CrossRef](#)]
22. Sandrock, T.; Diening, A.; Huber, G. Laser Emission of Erbium-Doped Fluoride Bulk Glasses in the Spectral Range from 2.7 to 2.8 μm. *Opt. Lett.* **1999**, *24*, 382–384. [[CrossRef](#)] [[PubMed](#)]
23. Wang, J.; Cheng, T.; Wang, L.; Yang, J.; Sun, D.; Yin, S.; Wu, X.; Jiang, H. Compensation of Strong Thermal Lensing in an LD Side-Pumped High-Power Er: YSGG Laser. *Laser Phys. Lett.* **2015**, *12*, 105004. [[CrossRef](#)]
24. Gao, S.; Chen, T.; Hu, M.; Xu, S.; Xiong, Y.; Cheng, S.; Zhang, W.; Wang, Y.; Yang, W. Effects of Er³⁺ Concentration on the Optical Properties of Er³⁺: SrGdGa₃O₇ Single Crystals. *Opt. Mater.* **2019**, *98*, 109502. [[CrossRef](#)]
25. Quan, C.; Sun, D.; Luo, J.; Zhang, H.; Fang, Z.; Zhao, X.; Hu, L.; Cheng, M.; Zhang, Q.; Yin, S. Growth, Structure and Spectroscopic Properties of Er, Pr: YAP Laser Crystal. *Opt. Mater.* **2018**, *84*, 59–65. [[CrossRef](#)]
26. Kang, S.; Yu, H.; Ouyang, T.; Chen, Q.; Huang, X.; Chen, Z.; Qiu, J.; Dong, G. Novel Er³⁺/Ho³⁺-Codoped Glass-Ceramic Fibers for Broadband Tunable Mid-Infrared Fiber Lasers. *J. Am. Ceram. Soc.* **2018**, *101*, 3956–3967. [[CrossRef](#)]
27. Wang, T.; Huang, F.; Ren, G.; Cao, W.; Tian, Y.; Lei, R.; Zhang, J.; Xu, S. Broadband 2.9 μm Emission and High Energy Transfer Efficiency in Er³⁺/Dy³⁺ Co-Doped Fluoroaluminate Glass. *Opt. Mater.* **2018**, *75*, 875–879. [[CrossRef](#)]
28. Tian, Y.; Li, B.; Wang, J.; Liu, Q.; Chen, Y.; Zhang, J.; Xu, S. The Mid-Infrared Emission Properties and Energy Transfer of Tm³⁺/Er³⁺ Co-Doped Tellurite Glass Pumped by 808/980 nm Laser Diodes. *J. Lumin.* **2019**, *214*, 116586. [[CrossRef](#)]
29. Chai, G.; Dong, G.; Qiu, J.; Zhang, Q.; Yang, Z. 2.7 μm Emission from Transparent Er³⁺, Tm³⁺ Codoped Yttrium Aluminum Garnet (Y₃Al₅O₁₂) Nanocrystals–Tellurate Glass Composites by Novel Comelting Technology. *J. Phys. Chem. C* **2012**, *116*, 19941–19950. [[CrossRef](#)]
30. Tian, Y.; Xu, R.; Hu, L.; Zhang, J. 2.7 μm Fluorescence Radiative Dynamics and Energy Transfer between Er³⁺ and Tm³⁺ Ions in Fluoride Glass under 800 Nm and 980 Nm Excitation. *J. Quant. Spectrosc. Radiat.* **2012**, *113*, 87–95. [[CrossRef](#)]
31. Cazorla, C.; Errandonea, D. Superionicity and polymorphism in calcium fluoride at high pressure. *Phys. Rev. Lett.* **2014**, *113*, 235902. [[CrossRef](#)]
32. Zhang, X.; Schulte, A.; Chai, B. Raman Spectroscopic Evidence for Isomorphous Structure of GdLiF₄ and YLiF₄ Laser Crystals. *Solid State Commun.* **1994**, *89*, 181–184. [[CrossRef](#)]
33. Zhao, C.; Hang, Y.; Zhang, L.; Yin, J.; Hu, P.; Ma, E. Polarized Spectroscopic Properties of Ho³⁺-Doped LuLiF₄ Single Crystal for 2 μm and 2.9 μm Lasers. *Opt. Mater.* **2011**, *33*, 1610–1615. [[CrossRef](#)]
34. Toncelli, A.; Tonelli, M.; Cassanho, A.; Jenssen, H. Spectroscopy and Dynamic Measurements of a Tm, Dy: BaY₂F₈ Crystal. *J. Lumin.* **1999**, *82*, 291–298. [[CrossRef](#)]
35. Cornacchia, F.; Toncelli, A.; Tonelli, M. 2-μm Lasers with Fluoride Crystals: Research and Development. *Prog. Quantum Electron.* **2009**, *33*, 61–109. [[CrossRef](#)]
36. Zhang, P.; Yin, J.; Zhang, B.; Zhang, L.; Hong, J.; He, J.; Hang, Y. Intense 2.8 μm Emission of Ho³⁺ Doped PbF₂ Single Crystal. *Opt. Lett.* **2014**, *39*, 3942–3945. [[CrossRef](#)] [[PubMed](#)]

37. Huang, X.; Wang, Y.; Zhang, P.; Su, Z.; Xu, J.; Xin, K.; Hang, Y.; Zhu, S.; Yin, H.; Li, Z. Efficiently Strengthen and Broaden 3 μm Fluorescence in PbF_2 Crystal by $\text{Er}^{3+}/\text{Ho}^{3+}$ as Co-Luminescence Centers and Pr^{3+} Deactivation. *J. Alloy. Compd.* **2019**, *811*, 152027. [[CrossRef](#)]
38. Kresse, G.; Hafner, J. Ab Initio Molecular Dynamics for Liquid Metals. *Phys. Rev. B* **1993**, *47*, 558. [[CrossRef](#)] [[PubMed](#)]
39. Kresse, G.; Furthmüller, J. Efficiency of Ab-Initio Total Energy Calculations for Metals and Semiconductors Using a Plane-Wave Basis Set. *Comp. Mater. Sci.* **1996**, *6*, 15–50. [[CrossRef](#)]
40. Blöchl, P.E. Projector Augmented-Wave Method. *Phys. Rev. B* **1994**, *50*, 17953. [[CrossRef](#)] [[PubMed](#)]
41. Perdew, J.P.; Burke, K.; Ernzerhof, M. Generalized Gradient Approximation Made Simple. *Phys. Rev. Lett.* **1996**, *77*, 3865. [[CrossRef](#)]
42. Ma, F.; Su, F.; Zhou, R.; Ou, Y.; Xie, L.; Liu, C.; Jiang, D.; Zhang, Z.; Wu, Q.; Su, L. The Defect Aggregation of Re^{3+} (Re = Y, La ~ Lu) in MF_2 (M = Ca, Sr, Ba) Fluorites. *Mater. Res. Bull.* **2020**, *125*, 110788. [[CrossRef](#)]
43. Aull, B.; Jenssen, H. Vibronic Interactions in Nd: YAG Resulting in Nonreciprocity of Absorption and Stimulated Emission Cross Sections. *IEEE J. Quantum Electron.* **1982**, *18*, 925–930. [[CrossRef](#)]
44. Zhang, W.; Wang, Y.; Li, J.F.; Zhu, Z.J.; You, Z.Y.; Tu, C.Y. Spectroscopic Properties and Rate Equation Model of Er Doped $\text{BaLaGa}_3\text{O}_7$ Crystals. *Mater. Res. Bull.* **2018**, *106*, 282–287. [[CrossRef](#)]
45. Liu, Y.; Wang, Y.; You, Z.; Li, J.; Zhu, Z.; Tu, C. Growth, Structure and Spectroscopic Properties of Melilite Er: $\text{CaLaGa}_3\text{O}_7$ Crystal for Use in Mid-Infrared Laser. *J. Alloy. Compd.* **2017**, *706*, 387–394. [[CrossRef](#)]
46. Zhang, J.Y.; Han, S.J.; Liu, L.T.; Yao, Q.; Dong, W.M.; Li, J. Crystal Structure and Judd–Ofelt Analysis of Er^{3+} Doped $\text{LuAl}_3(\text{BO}_3)_4$ Crystal. *Chin. Phys. Lett.* **2018**, *35*, 096101. [[CrossRef](#)]
47. Hou, W.; Xu, Z.; Zhao, H.; Xue, Y.; Wang, Q.; Xu, X.; Xu, J. Spectroscopic Analysis of Er: Y_2O_3 Crystal at 2.7 μm Mid-IR Laser. *Opt. Mater.* **2020**, *107*, 110017. [[CrossRef](#)]